AGU PUBLICATIONS

Geophysical Research Letters

RESEARCH LETTER
10.1002/2016GL069785

Key Points:
- Subducted seamount could induce complex thrust fault system, including distinct forethrust and backthrust faults
- With background horizontal compression due to backstop, subducted seamount might strengthen forethrust but suppress backthrust faults
- Inhomogeneous normal stress changes on seamount flanks and edges could contribute to the complexity of seamount-earthquake relationship

Supporting Information:
- Supporting Information S1
- Movie S1

Correspondence to:
J. Lin,
jlin@whoi.edu

Citation:
Ding, M., and J. Lin (2016), Deformation and faulting of subduction overriding plate caused by a subducted seamount, *Geophys. Res. Lett.*, *43*, 8936–8944, doi:10.1002/2016GL069785.

Received 7 JUN 2016
Accepted 15 AUG 2016
Accepted article online 16 AUG 2016
Published online 3 SEP 2016

Deformation and faulting of subduction overriding plate caused by a subducted seamount

Min Ding[1,2] and Jian Lin[3,4]

[1]MIT/WHOI Joint Program, Woods Hole Oceanographic Institution, Woods Hole, Massachusetts, USA, [2]Now at Department of Earth, Atmospheric, and Planetary Sciences, Massachusetts Institute of Technology, Cambridge, Massachusetts, USA, [3]Key Laboratory of Marginal Sea Geology, Chinese Academy of Sciences, South China Sea Institute of Oceanology, Guangzhou, China, [4]Department of Geology & Geophysics, Woods Hole Oceanographic Institution, Woods Hole, Massachusetts, USA

Abstract We conducted numerical experiments to simulate elastoplastic deformation of the overriding plate caused by a subducted seamount. Calculations revealed development of a distinct pair of fault-like shear zones, including a landward dipping forethrust fault initiated from the seamount top and a seaward dipping backthrust fault from the landward base of the seamount. Significant dome-shaped surface uplift was predicted above the thrust faults. Lesser-developed seaward dipping backthrust faults were calculated to develop under certain conditions. The overriding plate was calculated to deform in two stages: In *Stage I*, elastic deformation leads to the formation of fault-like shear zones. After major faults have cut through the entire plate, plastic deformation on faults dominates *Stage II*. On the subduction interface, compressional normal stress was calculated to increase on the landward leading flank of the seamount and decrease on the seaward trailing flank. These changes, together with associated stress singularities at seamount edges, could affect earthquake processes.

1. Introduction

Seamounts are ubiquitous features of ocean basins. The total number of seamounts has been estimated to be over 100,000 [*Wessel et al*., 2010] on the seafloor. Prominent examples of subducted seamounts have been imaged in multiple trenches, for example, the Nankai Trough off Japan [*Kodaira et al*., 2000], Gulf of Nicoya off Costa Rica [*Husen et al*., 2002], Hikurangi margin off New Zealand [*Bell et al*., 2010], and Cascadia subduction zone off Oregon [*Tréhu et al*., 2012].

Subducted seamounts could profoundly affect the morphology, stress state, and fault structure of the overriding plate. Laboratory sandbox experiments have shown complex uplift and subsidence patterns at different stages of seamount subduction [*Dominguez et al*., 2000]. Seismic reflection profiles on the Hikurangi margin off New Zealand [*Barnes et al*., 2010] revealed the existence of seamount-induced thrust faults, especially on the landward side of subducted seamounts. Seamounts also entrain fluid-rich sediments into great depths, increasing pore pressure and altering stress state of the overriding plate [e.g., *von Huene et al*., 2004].

Subducted seamounts could also affect megathrust earthquakes by altering stress state on the subduction interface. Subducted seamounts might either trigger megathrust events due to seamount geometry-related normal stress increase [*Cloos*, 1992; *Scholz and Small*, 1997; *Bilek et al*., 2003; *Yang et al*., 2013] or arrest megathrust events due to fluid-related decrease in the effective normal stress [*Kodaira et al*., 2000; *Robinson et al*., 2006; *Mochizuki et al*., 2008; *Yang et al*., 2012]. Furthermore, *Wang and Bilek* [2011, 2014] argued that the geometrical incompatibility of subducted seamounts could induce complex fault system and inhomogeneous stresses in the overriding plate, thus inhibiting megathrust events on the subduction interface and triggering microearthquakes of diverse stress orientations at various locations.

Although the complex fault pattern has been observed in sandbox experiments [*Dominguez et al*., 2000] and generalized in conceptual models [*Wang and Bilek*, 2011, 2014], the elastoplastic deformation of the overriding plate in response to subducted seamounts is still poorly understood. In this study, we conducted numerical experiments to quantify the seamount-induced overriding plate deformation and faulting. We also examined the stress evolution on the subduction interface and analyzed how the fault structure is influenced by a range of key parameters, including subduction dip angle, seamount slope, plate thickness, and internal and interface frictional angles.

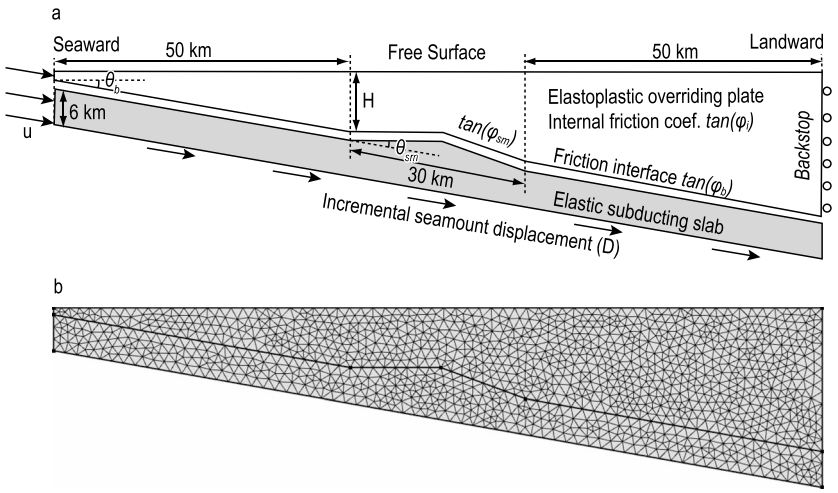

Figure 1. (a) Numerical model setup. (b) Finite-element triangular meshes.

2. Model Setup

Our 2-D model domain corresponds to the trench-perpendicular vertical cross section cutting through the center of a subducted seamount in a subduction zone, assuming plain strain condition (Figure 1a). The overriding plate is assumed to be elastoplastic obeying Mohr-Coulomb failure criteria. Most of our tested models assumed the internal frictional angle (φ_i) to be 0° (i.e., von Mises criteria). We varied three geometric parameters: Subduction dip angle (θ_b) in the range of 0–20°, seamount slope (θ_{sm}) of 5–25° [*Wessel*, 2001], and overriding plate thickness from the seaward base of the seamount (*H*) of 5–20 km. The subducting slab and seamount are assumed to be rigid by prescribing a Young's modulus 100 times that of the overriding plate to force the deformation to be localized in the overriding plate. Other parameters are shown in Figure 1a and Table S1.

The right side of the overriding plate is assumed to have zero horizontal displacement, analogous to a rigid backstop. The left side of the overriding plate moves together with the subducting slab. Both the right and left boundaries have limited influence on the seamount-related processes. The top boundary is stress free. The subduction interface is a frictional boundary with frictional angles $\varphi_{sm} = \text{atan}(\mu_{sm})$ along the seamount flanks and $\varphi_b = \text{atan}(\mu_b)$ for the rest of the subduction interface, where μ_{sm} and μ_b are corresponding friction coefficients. We tested φ_{sm} and φ_b from 0° to 30°. The upper limit corresponds to a frictional coefficient of 0.6 in Byerlee's law [*Byerlee*, 1978], while lower frictional angles are assumed to be due to higher pore pressure [*Davis et al*., 1983; *Saffer and Bekins*, 2002].

The seamount is assumed to always stick to the subducting slab, the down-dip movement of which was modeled by quasi-statically sweeping *D* from 0 to 1000 m. In order to incorporate gravity effect, we first calculated the deformation and lithostatic stress field caused by the gravity of the overriding plate by sweeping the gravity acceleration from zero to 9.8 m/s^2. All of the following results are fields of incremental stress and displacement after subtracting the gravity-induced fields. We used the finite-element software COMSOL Multiphysics 5.0 to conduct the numerical experiments. Triangular meshing schemes with a maximum element side length of 1 km (Figure 1b) were adopted to ensure the resolution of fault-like shear zones [*Gerbault et al*., 1998; *Buiter*, 2012].

3. Results

Here we discuss the system evolution of a reference model in its deformation, stress, faulting, and energy, followed by variations in the fault structure revealed through sensitivity tests.

3.1. Faulting, Deformation, Stress, and Energy Evolution

The reference model assumes θ_b =5°, θ_{sm} =10°, H = 10 km, and $\varphi_i = \varphi_{sm} = \varphi_b = 0°$, where φ_i of 0° is analogous to high pore fluid pressure. Frictional angles φ_{sm} and φ_b of 0° imply a frictionally uncoupled subduction interface, allowing the geometric anomaly of subducted seamount to be the only cause of stress localization and faulting.

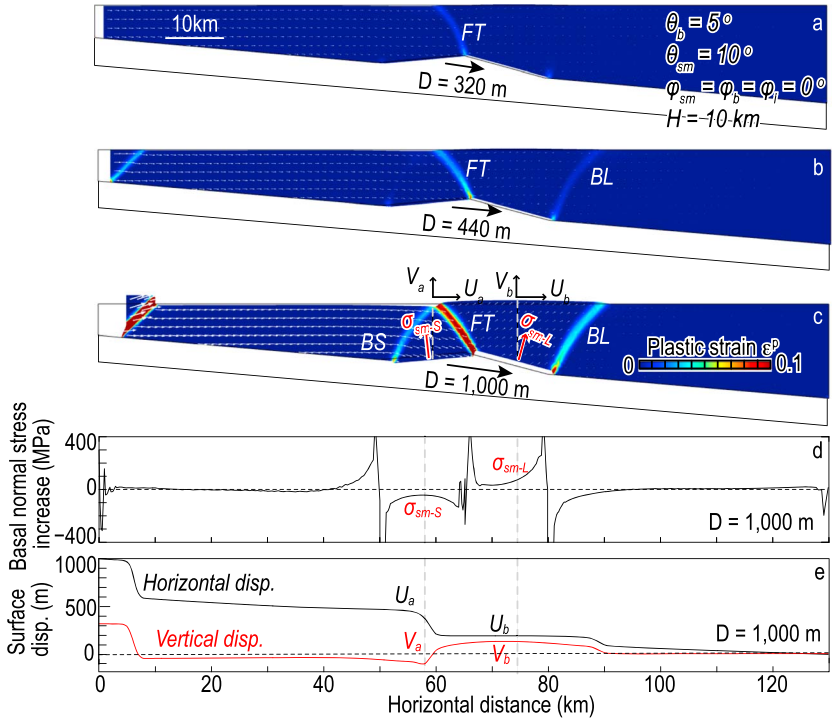

Figure 2. (a–c) Snapshots for the development of *FT*, *BL*, and *BS* in the reference model, with increasing *D*. Color indicates effective plastic strain ε_p, i.e., the second invariant of plastic strain tensor. Deformation is exaggerated by a factor of 5. Directions of V_a, V_b, U_a, U_b, $\sigma_{\text{sm-S}}$, and $\sigma_{\text{sm-L}}$ are marked in corresponding locations. (d) Compressional normal stress changes along subduction interface when $D = 1000$ m. $\sigma_{\text{sm-S}}$ and $\sigma_{\text{sm-L}}$ are maximum stress changes on seamount flanks. (e) Surface deformation when $D = 1000$ m. V_a and V_b are vertical deformation, while U_a and U_b are horizontal deformation for points *a* and *b*, respectively.

Seamount edges induce strong stress concentration, initiating three faults sequentially (Figures 2a–2c and Movie S1). A landward dipping forethrust fault *FT* (thin shear zone in Figure 2a) was calculated to first initiate from the seamount top and gradually cut through the entire plate where the overriding lithosphere is the thinnest. A seaward dipping backthrust fault *BL* (Figure 2b) then develops from the landward base of the seamount, also gradually cutting through the entire plate. A lesser-developed backthrust fault *BS* (Figure 2c) subsequently develops from the seaward base of the seamount. The corresponding seamount movement (*D*) when *FT*, *BL*, and *BS* cut through the entire plate were measured as $D_{\text{FT}} = 230$ m, $D_{\text{BL}} = 300$ m, and $D_{\text{BS}} = 460$ m, respectively (Figure 3b). The fault dip angles (α) were measured to be 43°–49° with an uncertainty of ~2–3° (Table S2). Over *FT* and *BL*, a dome-shaped region with significant uplift was predicted (Figures 2c and 2e). A seaward region with slight subsidence was also calculated over *FT* and *BS*. The calculated maximum subsidence V_a (at point a) and maximum uplift V_b (at point b) were about 9% and 11% of the seamount movement (*D*) (Figure 3c and Table S2).

Compressional normal stress was calculated to increase along the landward leading flank of the seamount while decreasing on the seaward trailing flank (Figure 2d). Stress singularities were predicted at the seamount edges where faults initiate. The normal stress along the landward leading flank $\sigma_{\text{sm-L}}$ increases to a steady state value of ~50 MPa after *FT* and *BL* fully develop (Figure 3b). In contrast, the normal stress along the seaward trailing flank $\sigma_{\text{sm-S}}$ decreases to a steady state value of ~−44 MPa after *BS* fully develops. The energy of the system evolves in two stages (Figure 3d). In *Stage I* (before D_{c1} of 380 m), elastic energy ΔE accumulates rapidly. In *Stage II* (after D_{c1} is reached), plastic dissipation energy ΔP increases, eventually reaching the value of ΔE at $D_{c2} = 640$ m.

3.2. Fault Structure

We tested 17 numerical models (Table S2) to systematically explore the fault structure as influenced by six parameters, θ_b, θ_{sm}, *H*, φ_i, φ_{sm}, and φ_b. We varied only one parameter each time, keeping other parameters to be the same as in the reference model.

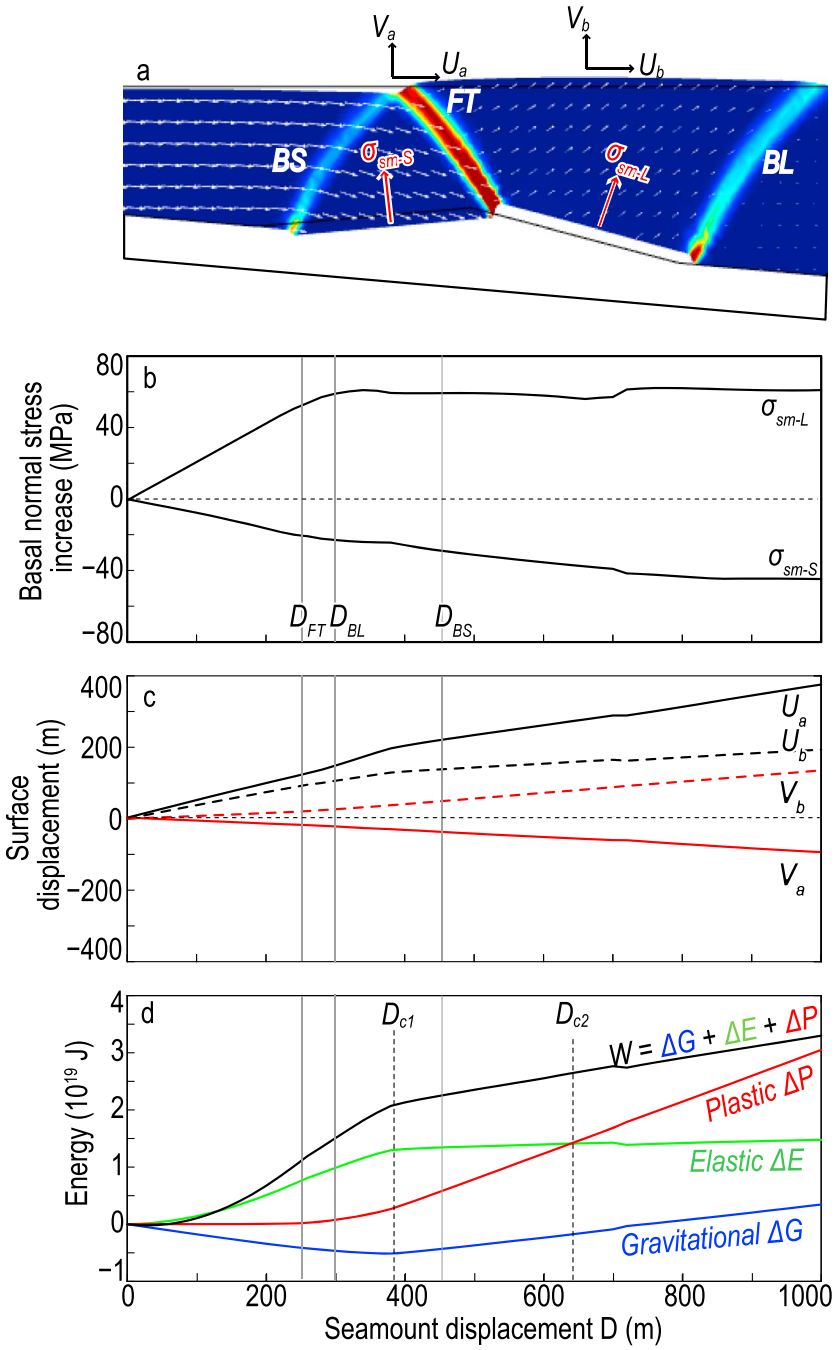

Figure 3. (a) Enlarged final fault structure in Figure 2c. Color indicates effective plastic strain. Red and black arrows indicate directions of $\sigma_{sm\text{-}S}$, $\sigma_{sm\text{-}L}$, V_a, V_b, U_a, and U_b. White arrows are deformation vectors, exaggerated by a factor of 3. (b) Evolution of $\sigma_{sm\text{-}S}$ and $\sigma_{sm\text{-}L}$. (c) Evolution of V_a, V_b, U_a, and U_b. (d) Evolution of energy, decomposed into elastic energy ΔE, plastic dissipation energy ΔP, and gravitational potential energy ΔG.

The common features include two prominent faults *FT* and *BL*, while lesser-developed seaward dipping backthrust faults *BS* and *BT* were calculated to develop under certain conditions. For models with varied subduction dip angle θ_b (Models 1a–1f in Table S2), *BT* was calculated to develop from the top of the seamount for a low θ_b of 0 and 2.5° (Figures 4a and S1a–S1b), while *BS* was calculated to develop from the seamount seaward base for a higher θ_b of 2.5–20° (Figures 3a and S1c–S1f). For models with varied seamount slope θ_{sm} (Models 2a–2f in Table S2), *BS* develops for a low θ_{sm} of 5–15° (Figures 3a and S2b–S2d), while *BT* develops for a high

θ_{sm} of 20–25° (Figures 4b and S2e–S2f). Thus, whether *BS* or *BT* develops for given θ_b and θ_{sm} values is primarily controlled by whether the landward side or the top of the seamount is more easily fractured.

Greater friction along the subduction interface enhances the coupling between the subducting and overriding plates, thus reducing the relative importance of the seamount in stress localization and faulting. For our tested models with frictional angles $\varphi_{sm} = \varphi_b = 10$, 20, and 30° (Models 4b–4d in Table S2), only the two prominent faults *FT* and *BL* develop with limited amount of plastic strain (Figure 4c). We also tested cases where seamount flanks have different friction from the rest of the plate interface. When a higher frictional angle (i.e., $\varphi_{sm} > \varphi_b$) was applied to the seamount flanks, a pair of conjugate thrust faults develop from the landward base of the seamount (Figure 4d). This corresponds to the situation when the seamount flanks are associated with relatively rough interface, less sediment thickness, or fewer trapped fluids. In comparison, if $\varphi_{sm} < \varphi_b$, no fault develops. The required seamount displacement for the fault system to be fully developed (D_{c2}) is larger for deeper seamount, larger subduction dipping angle, and larger subduction interface friction (Table S2 and Figure S5).

4. Discussion

Our numerical results quantified the influence of a subducted seamount on the elastoplastic deformation and stress evolution of the overriding plate, providing insights on the observable surface deformation, fault structure, and potential influence on earthquake processes.

4.1. Fault System Evolution

Our models examined the initiation and early stages of fault evolution caused by a finite seamount movement. Dividing our modeled seamount displacement of 1000 m by a subduction rate of 2–8 cm/yr yields a corresponding time scale of 12,500–50,000 years. In contrast, the time period for a seamount to subduct beneath a 50–200 km wide accretionary wedge [*Clift and Vannucchi*, 2004] is ~$0.5–10 \times 10^6$ years, long enough for the seamount to severely deform and fracture the overriding plate along its subduction path, initiating new faults and reactivating old faults as observed in sandbox experiments [*Dominguez et al*., 1998, 2000]. The formation of a pair of conjugate thrust faults identified in our numerical models might be repeated episodically at various depths along the subduction path of the seamount, producing a complex fault system.

4.2. Seismic Profiles, Subduction Zone Tectonics, and Sandbox Experiments

Our predicted horizontal compression and thrust faults are consistent with the seismic observation on the accretionary Hikurangi margin, New Zealand [*Barnes et al*., 2010], where forethrust and backthrust faults were found near multiple subducted seamounts. Accretionary margins are characterized by horizontal compression with pervasive forethrust faults (Figure 5a) [*Dahlen*, 1990; *Clift and Vannucchi*, 2004; *Buiter*, 2012]. We expect that the combination of background compression and seamount-induced stresses (Figure 5b) to strengthen forethrust faults in the neighborhood of seamounts [*Ellis et al*., 2014] but to suppress backthrust faults (Figure 5c). Seamount-induced backthrust faults may only develop when the forethrust faults cannot fully release seamount-induced stresses. However, our models cannot be directly applied to nonaccretionary wedges due to a different background stress state. For example, background horizontal extension has been inferred from the overwhelming normal faults in seismic profiles of the Mariana subduction zone [*Hussong and Uyeda*, 1981; *Chapp et al*., 2008]. *Oakley et al*. [2008] further reported no visible seamount-associated faults in the Mariana overriding plate, probably due to high-level serpentinization, abrupt change in the plate dip [*ten Brink*, 2005], and significant degradation of subducted seamounts. Even if a seamount could effectively disturb the overriding plate, the overwhelming horizontal extension in nonaccretionary subduction zones may prefer normal faults to accommodate for the seamount subduction [*Fryer et al*., 1985].

We considered the situation when the seamount sticks to the subducting slab with limited amount of internal deformation. In reality, the relative strength of the seamount with respect to the surrounding materials controls whether it could be deformed, fractured [*Baba et al*., 2001], jammed, or even truncated [*Cloos and Shreve*, 1996]. As accretionary wedge sediments are gradually condensed and dehydrated to become seismogenic materials [*Moore and Saffer*, 2001], the seamount becomes harder to subduct to great depth. However, subducted seamounts identified in seismic profiles [e.g., *Ellis et al*., 2015] support the assumption that some

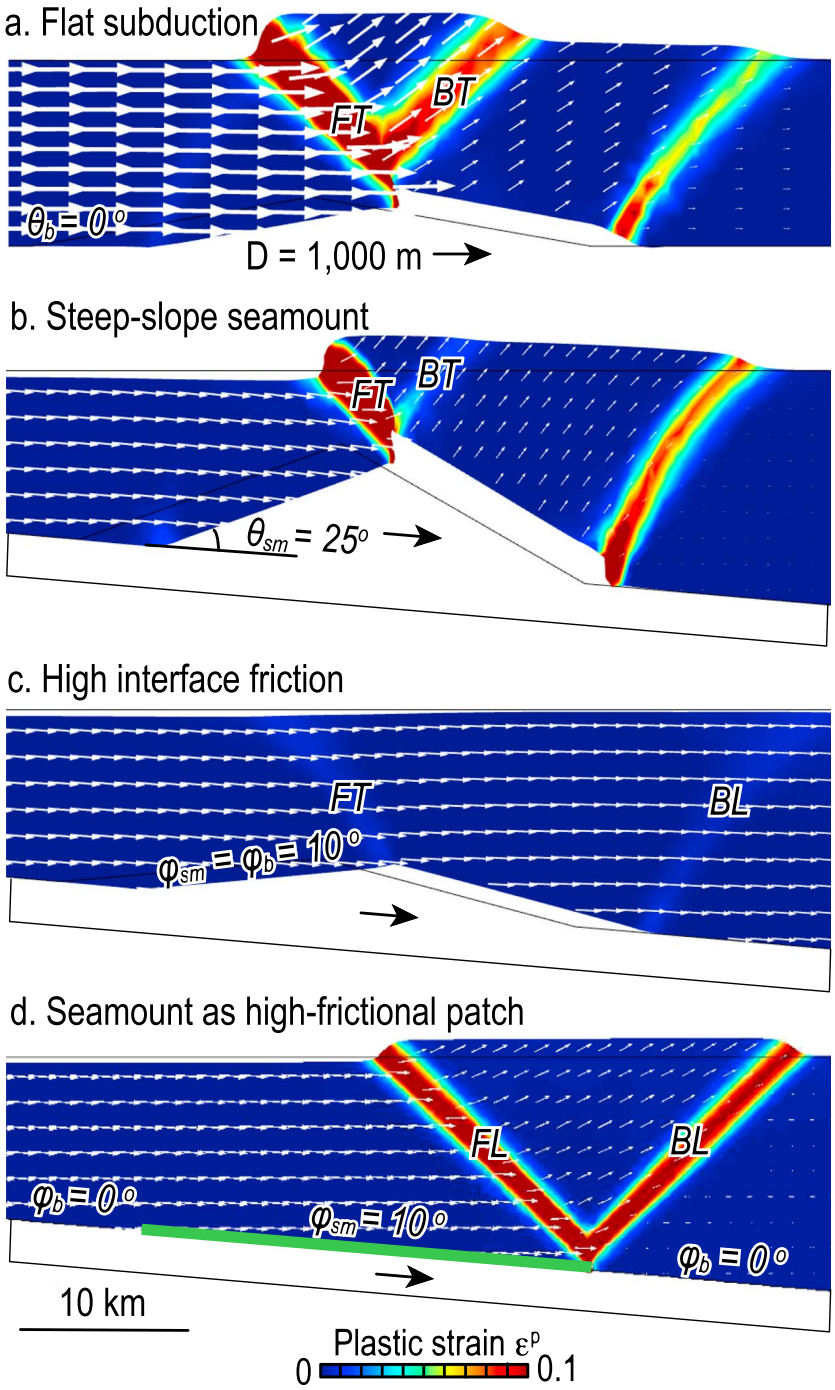

Figure 4. Fault structure identified in sensitivity tests, showing as snapshots when $D = 1000$ m. Color indicates effective plastic strain. White arrows are deformation vectors, exaggerated by a factor of 3. (a and b) For flat subduction ($\theta_b = 0°$) or steep-slope seamount ($\theta_{sm} = 25°$), *BT* develops in addition to *FT* and *BL*. (c) For nonzero frictional angle for the entire subduction interface (e.g., $\phi_{sm} = \phi_b = 10°$ or larger), only *FT* and *BL* develop. (d) Approximating the seamount as high frictional patch (bold green line, $\phi_{sm} = 10°$, $\phi_b = 0°$) without geometric anomaly, conjugate thrust faults *FL* and *BL* develop simultaneously from the landward base of the seamount.

subducted seamounts are strong enough to enter seismogenic depth and continue influencing the overriding plate. The flexural response of the subducting slab and seamount to the overriding plate [*Scholz and Small*, 1997] is not included here as this vertical adjustment is considered to be less significant than the horizontal shearing [*Cloos*, 1993].

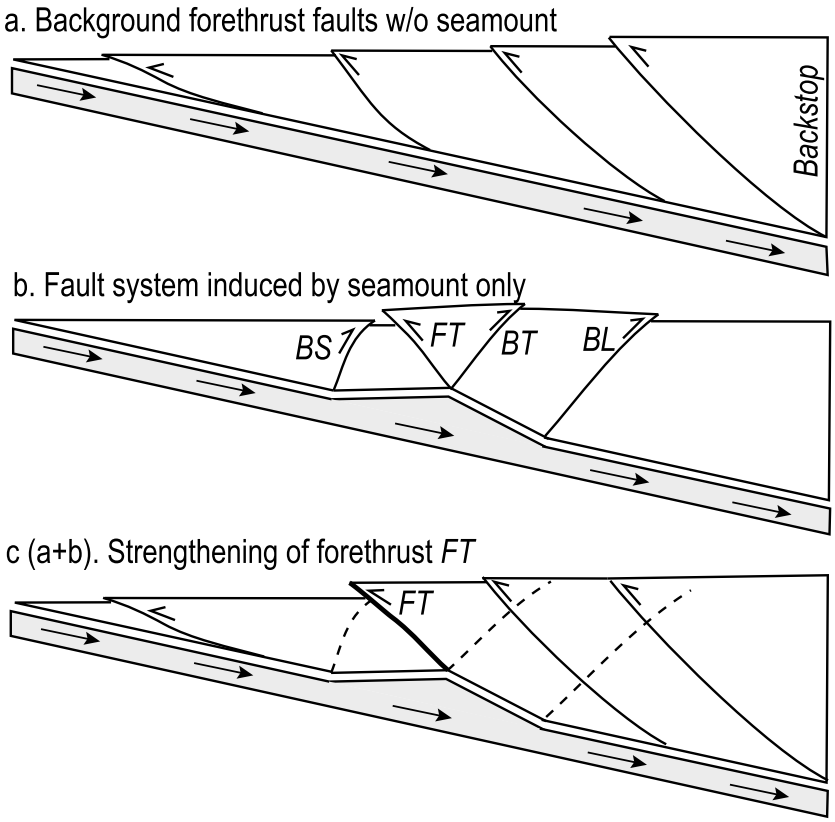

Figure 5. (a) Sketch of forethrust faults in an accretionary wedge based on geologic and drilling observations [*Dahlen*, 1990] and numerical simulations [*Buiter*, 2012]. (b) Simulated seamount-induced fault system in this study. (c) Illustration of the expectation that the combination of Figures 5a and 5b could strengthen forethrust faults (bold line) but suppress backthrust faults (dashed lines).

Sandbox experiments [*Dominguez et al*., 1998, 2000] showed thrust faults in front of the seamount and normal faults behind the seamount, consistent with critical taper theory [e.g., *Dahlen*, 1990; *Suppe*, 2007; *Buiter*, 2012] and stability analysis [*Lallemand and Pichon*, 1987]. We hypothesize that the difference in the predicted fault type behind the seamount is primarily due to material properties: Sands are close to failure everywhere and therefore could accommodate the movement of a subducted seamount by material subsidence and normal faults behind the seamount. In contrast, our assumed elastoplastic material is in transition from elastic to plastic failure, whose deformation tends to be localized within a limited number of fault-like shear zones.

4.3. Interaction Between Fluids and Forearc Faults

Dehydration of subducted sediments [*Peacock*, 1990] provides highly overpressured fluids both within the overriding plate and on the subduction interface. Elevated pore pressure and reduced effective normal stress have been suggested to influence a wide range of subduction zone forearc structures and faulting processes [e.g., *Moore and Vrolijk*, 1992; *Saffer and Tobin*, 2011]. Drilling and seismic studies [e.g., *Bangs et al*., 2014] have shown spatial and temporal heterogeneities in the subduction zone fluid flow, contributing to complex friction and seismogenic behaviors on the subduction interface. Our numerical models capture the main influence of fluids on facilitating the formation of seamount-induced faults by reducing both the internal friction and basal friction angles [*Strayer et al*., 2001]. In another aspect, faults could influence the hydrogeology in the overriding plate by providing fluid escape channels. If high pore pressure and low effective friction exist on preexisting fault zones [*Tsuji et al*., 2014], we speculate that the fault formation processes, whether induced by subducted seamounts or not, can been influenced by preferring reactivating preexisting faults to initiating new faults.

4.4. Influence on Megathrust Earthquakes

There is a debate on whether subducted seamounts might trigger [*Cloos*, 1992; *Scholz and Small*, 1997; *Bilek et al*., 2003; *Yang et al*., 2013] or retard megaearthquakes [*Kodaira et al*., 2000; *Robinson et al*., 2006; *Mochizuki*

et al., 2008; *Yang et al*., 2012]. Various studies have attributed the triggering to increased normal stress on the seamount flanks; others have attributed the retardation to entrained fluid-rich sediments. However, these studies ignore the fault structure caused by seamount subduction [*Wang and Bilek*, 2011, 2014]. Our study suggests that although the normal stress might be increased on the landward leading flank of the seamount, it is reduced on the seaward trailing flank. Therefore, earthquakes might be triggered on the landward leading flank and retarded on the seaward trailing flank, together contributing to the observed complexity of seamount-earthquake relationship. In addition, the calculated stress singularities at the seamount edges could greatly enhance the stress heterogeneity and inhibit the propagation of megathrust earthquakes [*Wang and Bilek*, 2014].

4.5. Implications for 3-D Fault Structure

Our 2-D numerical results are an approximation of a trench-perpendicular vertical cross section cutting through the center of a 3-D seamount (CC′ in Figure S6a). Preliminary results of a 3-D seamount subduction model, assuming the same parameter values as in the 2-D reference model, show the seamount-induced thrust faults *BS*, *FT*, and *BL*, being consistent with the 2-D results (compare Figure S6e with Figure S6f). In addition, the calculated 3-D surface deformation and basal stress changes along the vertical cross-section CC′ are also consistent with the 2-D results (Figures S6h and S6i). On the map view, the 3-D seamount induces a significant dome-shaped uplift in front of the seamount and subsidence behind the seamount (Figure S6d), as well as significant normal stress increase on the landward leading flank of the seamount and decrease on the seaward trailing flank (Figure S6c), again being consistent with the 2-D results. Systematic investigation of 3-D effects is the subject of ongoing and future studies.

5. Conclusions

Our 2-D numerical models quantify the elastoplastic deformation and faulting in the overriding plate caused by a subducted seamount, yielding the following results:

1. A landward dipping forethrust fault was calculated to first initiate from the top of the seamount, followed by a seaward dipping backthrust fault from the landward base of the seamount. Significant surface uplift was predicted over the two thrust faults. Lesser-developed backthrust fault may originate from the top or seaward base of the seamount. The required seamount displacement for the fault system to fully develop is larger for deeper seamount, larger subduction dipping angle, and larger subduction interface friction.
2. The compressional normal stress was calculated to increase on the landward leading flank and decrease on the seaward trailing flank of the seamount. Stress singularities occur at the seamount edges where fault zones originate.
3. Deformation and energy of the system were calculated to evolve in two stages. Elastic deformation and energy accumulation dominate *Stage I* before the major thrust faults cut through entire plate. This is followed by *Stage II* with significant plastic deformation and energy dissipation within fault zones.

Acknowledgments
This study benefitted from discussion with Mark Behn, Jean-Arthur Olive, Hongfeng Yang, Jeff McGuire, Brian Tucholke, Dan Bassett, Charles Williams, Kelin Wang, Julia Morgan, Gary Gray, Wey Yi Foo, Susan Ellis, and Mark Cloos. We thank Srikanth Vaidianathan for technical support. This work is supported by NSF grant OCE-1141785 and Mariana Trench Initiative of SCSIO (J.L.) and a WHOI DOEI Graduate Student Fellowship (M.D.). The COMSOL Multiphysics software is available at https://www.comsol.com/. The data and input files necessary to reproduce the numerical experiments are available from the authors upon request (jlin@whoi.edu).

References

Baba, T., T. Hori, S. Hirano, P. R. Cummins, J. Park, M. Kameyama, and Y. Kaneda (2001), Deformation of a seamount subducting beneath an accretionary prism: Constraints from numerical simulation, *Geophys. Res. Lett.*, *28*, 1827–1830, doi:10.1029/2000GL012266.

Bangs, N. L., K. D. McIntosh, E. A. Silver, J. W. Kluesner, and C. R. Ranero (2014), Fluid accumulation along the Costa Rica subduction thrust and development of the seismogenic zone, *J. Geophys. Res. Solid Earth*, *120*, 67–86, doi:10.1002/2014JB011265.

Barnes, P. M., G. Lamarche, J. Bialas, S. Henrys, I. Pecher, G. L. Netzeband, J. Greinert, J. J. Mountjoy, K. Pedley, and G. Crutchley (2010), Tectonic and geological framework for gas hydrates and cold seeps on the Hikurangi subduction margin, New Zealand, *Mar. Geol.*, *272*, 26–48, doi:10.1016/j.margeo.2009.03.012.

Bell, R., R. Sutherland, D. H. N. Barker, S. Henrys, S. Bannister, L. Wallace, and J. Beavan (2010), Seismic reflection character of the Hikurangi subduction interface, New Zealand, in the region of repeated Gisborne slow slip events, *Geophys. J. Int.*, *180*, 34–48, doi:10.1111/j.1365-246X.2009.04401.x.

Bilek, S. L., S. Y. Schwartz, and H. R. DeShon (2003), Control of seafloor roughness on earthquake rupture behavior, *Geology*, *31*, 455–458.

Buiter, S. J. H. (2012), A review of brittle compressional wedge models, *Tectonophysics*, *530-531*, 1–17, doi:10.1016/j.tecto.2011.12.018.

Byerlee, J. (1978), Friction of rocks, *Pure Appl. Geophys.*, *116*, 615–626.

Chapp, E., B. Taylor, A. Oakley, and G. F. Moore (2008), A seismic stratigraphic analysis of Mariana forearc basin evolution, *Geochem. Geophys. Geosyst.*, *9*, Q10X02, doi:10.1029/2008GC001998.

Clift, P., and P. Vannucchi (2004), Controls on tectonic accretion versus erosion in subduction zones: Implications for the origin and recycling of the continental crust, *Rev. Geophys.*, *42*, RG2001, doi:10.1029/2003RG000127.

Cloos, M. (1992), Thrust-type subduction-zone earthquakes and seamount asperities: A physical model for seismic rupture, *Geology*, *20*, 601–604, doi:10.1130/0091-7613.

Cloos, M. (1993), Lithospheric buoyancy and collisional orogenesis: Subduction of oceanic plateaus, continental margins, island arcs, spreading ridges, and seamounts, *Geol. Soc. Am. Bull.*, *105*, 715–737, doi:10.1130/0016-7606(1993)105<0715:LBACOS>2.3.CO;2.
Cloos, M., and R. L. Shreve (1996), Shear-zone thickness and the seismicity of Chilean- and Marianas-type subduction zones, *Geology*, *24*, 107–110, doi:10.1130/0091-7613(1996)024<0107:SZTATS>2.3.CO;2.
Dahlen, F. A. (1990), Critical taper model of fold-and-thrust belts and accretionary wedges, *Annu. Rev. Earth Planet. Sci.*, *18*, 55–99, doi:10.1146/annurev.ea.18.050190.000415.
Davis, D., J. Suppe, and F. A. Dahlen (1983), Mechanics of fold-and-thrust belts and accretionary wedges, *J. Geophys. Res.*, *88*, 1153–1172, doi:10.1029/JB088iB02p01153.
Dominguez, S., S. Lallemand, J. Malavieille, and R. von Huene (1998), Upper plate deformation associated with seamount subduction, *Tectonophysics*, *293*, 207–224, doi:10.1016/S0040-1951(98)00086-9.
Dominguez, S., J. Malavieille, and S. E. Lallemand (2000), Deformation of accretionary wedges in response to seamount subduction: Insights from sandbox experiments, *Tectonics*, *19*, 182–196, doi:10.1029/1999TC900055.
Ellis, S., F. Ghisetti, P. Barnes, A. Reyes, A. Fagereng, F. Henrys, D. Baker, and S. Henrys (2014), Numerical experiments into the style of accretion and megathrust behavior along the Hikurangi margin, New Zealand Abstract T51A-4596, presented at 2014 Fall Meeting, AGU, San Francisco, Calif., 15–19 Dec.
Ellis, S., Å. Fagereng, D. Barker, S. Henrys, D. Saffer, L. Wallace, C. Williams, and R. Harris (2015), Fluid budgets along the northern Hikurangi subduction margin, New Zealand: The effect of a subducting seamount on fluid pressure, *Geophys. J. Int.*, *202*, 277–297, doi:10.1093/gji/ggv127.
Fryer, P., E. L. Ambos, and D. M. Hussong (1985), Origin and emplacement of Mariana forearc seamounts, *Geology*, *13*, 774–777, doi:10.1130/0091-7613(1985)13<774:OAEOMF>2.0.CO;2.
Gerbault, M., A. N. B. Poliakov, and M. Daignieres (1998), Prediction of faulting from the theories of elasticity and plasticity: What are the limits?, *J. Struct. Geol.*, *20*, 301–320, doi:10.1016/S0191-8141(97)00089-8.
Husen, S., E. Kissling, and R. Quintero (2002), Tomographic evidence for a subducted seamount beneath the Gulf of Nicoya, Costa Rica: The cause of the 1990 Mw = 7.0 Gulf of Nicoya earthquake, *Geophys. Res. Lett.*, *29*(8), 1238, doi:10.1029/2001GL014045.
Hussong, D. M., and S. Uyeda (1981), Tectonic processes and the history of the Mariana arc: A synthesis of the results of Deep Sea Drilling Project Leg 60, *Initial Rep. Deep Sea Drill. Proj.*, *60*, 909–929.
Kodaira, S., N. Takahashi, A. Nakanishi, S. Miura, and Y. Kaneda (2000), Subducted seamount imaged in the rupture zone of the 1946 Nankaido earthquake, *Science*, *289*, 104–106, doi:10.1126/science.289.5476.104.
Lallemand, S., and X. L. Pichon (1987), Coulomb wedge model applied to the subduction of seamounts in the Japan Trench, *Geology*, *15*, 1065–1069, doi:10.1130/0091-7613(1987)15<1065:CWMATT>2.0.CO;2.
Mochizuki, K., T. Yamada, M. Shinohara, Y. Yamanaka, and T. Kanazawa (2008), Weak interplate coupling by seamounts and repeating $M \sim 7$ earthquakes, *Science*, *321*, 1194–1197, doi:10.1126/science.1160250.
Moore, J. C., and D. Saffer (2001), Updip limit of the seismogenic zone beneath the accretionary prism of southwest Japan: An effect of diagenetic to low-grade metamorphic processes and increasing effective stress, *Geology*, *29*, 183–186, doi:10.1130/0091-7613(2001)029<0183:ULOTSZ>2.0.CO;2.
Moore, J. C., and P. Vrolijk (1992), Fluids in accretionary prisms, *Rev. Geophys.*, *30*, 113–135, doi:10.1029/92RG00201.
Oakley, A. J., B. Taylor, and G. F. Moore (2008), Pacific Plate subduction beneath the central Mariana and Izu-Bonin fore arcs: New insights from an old margin, *Geochem. Geophys. Geosyst.*, *9*, Q06003, doi:10.1029/2007GC001820.
Peacock, S. A. (1990), Fluid processes in subduction zones, *Science*, *248*, 329–337.
Robinson, D. P., S. Das, and A. B. Watts (2006), Earthquake rupture stalled by a subducting fracture zone, *Science*, *312*, 1203–1205, doi:10.1126/science.1125771.
Saffer, D. M., and B. A. Bekins (2002), Hydrologic controls on the morphology and mechanics of accretionary wedges, *Geology*, *30*, 271–274, doi:10.1130/0091-7613(2002)030.
Saffer, D. M., and H. J. Tobin (2011), Hydrogeology and mechanics of subduction zone forearcs: Fluid flow and pore pressure, *Annu. Rev. Earth Planet Sci.*, *39*, 157–186, doi:10.1146/annurev-earth-040610-133408.
Scholz, C. H., and C. Small (1997), The effect of seamount subduction on seismic coupling, *Geology*, *25*, 487–490, doi:10.1130/0091-7613.
Strayer, L. M., P. J. Hudleston, and L. J. Lorig (2001), A numerical model of deformation and fluid-flow in an evolving thrust wedge, *Tectonophysics*, *335*, 121–145, doi:10.1016/S0040-1951(01)00052-X.
Suppe, J. (2007), Absolute fault and crustal strength from wedge tapers, *Geology*, *35*, 1127–1130, doi:10.1130/G24053A.1.
ten Brink, U. (2005), Vertical motions of the Puerto Rico Trench and Puerto Rico and their cause, *J. Geophys. Res.*, *110*, B06404, doi:10.1029/2004JB003459.
Tréhu, A. M., R. J. Blakely, and M. C. Williams (2012), Subducted seamounts and recent earthquakes beneath the central Cascadia forearc, *Geology*, *40*, 103–106, doi:10.1130/G32460.1.
Tsuji, T., R. Kamei, and R. G. Pratt (2014), Pore pressure distribution of a mega-splay fault system in the Nankai Trough subduction zone: Insight into up-dip extent of the seismogenic zone, *Earth Planet. Sci. Lett.*, *396*, 165–178, doi:10.1016/j.epsl.2014.04.011.
von Huene, R., C. R. Ranero, and P. Vannucchi (2004), Generic model of subduction erosion, *Geology*, *32*, 913–916, doi:10.1130/G20563.1.
Wang, K., and S. L. Bilek (2011), Do subducting seamounts generate or stop large earthquakes?, *Geology*, *39*, 819–822, doi:10.1130/G31856.1.
Wang, K., and S. L. Bilek (2014), Fault creep caused by subduction of rough seafloor relief, *Tectonophysics*, *610*, 1–24, doi:10.1016/j.tecto.2013.11.024.
Wessel, P. (2001), Global distribution of seamounts inferred from gridded Geosat/ERS-1 altimetry, *J. Geophys. Res.*, *106*, 19,431–19,442, doi:10.1029/2000JB000083.
Wessel, P., D. T. Sandwell, and S.-S. Kim (2010), The global seamount census, *Oceanografia*, *23*, 24–33.
Yang, H., Y. Liu, and J. Lin (2012), Effects of subducted seamounts on megathrust earthquake nucleation and rupture propagation, *Geophys. Res. Lett.*, *39*, L24302, doi:10.1029/2012GL053892.
Yang, H., Y. Liu, and J. Lin (2013), Geometrical effects of a subducted seamount on stopping megathrust ruptures, *Geophys. Res. Lett.*, *40*, 1–6, doi:10.1002/grl.50509.